International Journal of Trend in Scientific Research and Development (IJTSRD)
Volume 10 Issue 3, May-Jun 2026 Available Online: www.ijtsrd.com e-ISSN: 2456 – 6470

Solid-State Synthesis and Ionic Conductivity of Perovskite-Type Oxides

Professor (Dr). Dilip Kumar Choudhary

Head of the Department of Chemistry, L. N. Mithila University Darbhanga and Dean, Faculty of Science, L. N. Mithila University, Darbhanga, Bihar, India

ABSTRACT

Perovskite-type oxides with the general formula ABO3 have attracted considerable attention as prospective electrolyte and electrode materials in solid oxide fuel cells (SOFCs), oxygen separation membranes, and electrochemical sensors due to their structural versatility and tunable ionic transport properties. In this study, three representative lanthanum-based perovskite compositions- $La^{0.8}Sr^{0.2}MnO^3$, $La^{0.7}Sr^{0.3}CoO^3$, and $LaFeO^3$-were synthesized via conventional high-temperature solid-state reaction. Phase purity was confirmed by X-ray diffraction (XRD) analysis, and microstructural characterization was performed using scanning electron microscopy (SEM). Ionic conductivity was evaluated over the temperature range of 600–1000 K using electrochemical impedance spectroscopy (EIS). Activation energies derived from Arrhenius analysis ranged from 0.55 to 0.82 eV, with $La^{0.7}Sr^{0.3}CoO^3$ exhibiting the highest conductivity of 3.8×10^{-2} S cm^{-1} at 900 K. The influence of A-site Sr2+ substitution on oxygen vacancy concentration and consequent ionic transport is discussed in the framework of defect chemistry and Goldschmidt tolerance factor analysis. These findings underscore the potential of Sr-doped lanthanum perovskites as high-performance solid electrolytes for intermediate-temperature energy conversion devices.

KEYWORDS: *perovskite oxides; solid-state synthesis; ionic conductivity; electrochemical impedance spectroscopy; solid oxide fuel cells; oxygen vacancies; Arrhenius analysis.*

How to cite this paper: Professor (Dr). Dilip Kumar Choudhary "Solid-State Synthesis and Ionic Conductivity of Perovskite-Type Oxides" Published in International Journal of Trend in Scientific Research and Development (ijtsrd), ISSN: 2456-6470, Volume-10 | Issue-3, June 2026, pp.1195-1200, URL: www.ijtsrd.com/papers/ijtsrd125040.pdf

IJTSRD125040

1. INTRODUCTION

Perovskite oxides, characterized by the general formula ABO_3 where A is a large-radius alkaline earth or rare-earth cation and B is a smaller transition metal cation, represent one of the most structurally accommodating oxide families known to materials science (Mitchell, 2002). Their crystal architecture tolerates extensive compositional substitution at both cation sites, enabling the systematic engineering of electronic, magnetic, and ionic transport properties through targeted doping strategies (Tejuca & Fierro, 1993). This compositional flexibility, combined with thermodynamic stability at elevated temperatures and compatibility with ceramic processing routes, positions perovskite oxides as compelling candidates for a wide spectrum of energy-related applications.

The global energy transition has intensified the search for oxide ion and proton conductors capable of operating efficiently at intermediate temperatures (500–800 °C). Solid oxide fuel cells (SOFCs) employing perovskite electrolytes and mixed ionic–electronic conducting (MIEC) electrodes have demonstrated power densities exceeding 1 W cm^{-2} at reduced operating temperatures (Bi et al., 2019). Meanwhile, $La_{1-x}Sr_xMnO_3$ (LSM) and $La_{1-x}Sr_xCoO_{3-\delta}$ (LSC) composites continue to dominate SOFC cathode research owing to their high electronic conductivity and moderate oxygen exchange kinetics (Adler, 2004). Central to exploiting these materials is a detailed understanding of the mechanisms that govern ionic migration within the perovskite lattice.

Ionic transport in ABO_3 perovskites proceeds predominantly via oxygen vacancy hopping, a thermally activated process whose rate is governed by the concentration and mobility of oxygen vacancies (Goodenough, 2003). Vacancy formation can be enhanced through deliberate aliovalent substitution;

replacing trivalent La^{3+} with divalent Sr^{2+} introduces charge imbalance that is compensated by the creation of doubly charged oxygen vacancies (Vö), as described by Kröger–Vink notation. However, excessive doping can lead to vacancy ordering, secondary phase precipitation, and ultimately diminished conductivity (Kilner, 2008). Identifying the optimal doping level therefore remains an active research challenge.

Solid-state reaction routes, despite their simplicity, impose stringent demands on precursor particle size, homogeneity, and calcination protocol. High temperatures and prolonged sintering durations required for diffusion-limited reactions can promote grain growth and secondary phase formation, adversely affecting electrochemical performance (West, 2014). Understanding the interplay between synthesis parameters-calcination temperature, atmosphere, dwell time-and the resulting phase purity, microstructure, and ionic transport is therefore crucial for rational process design.

The present investigation addresses these considerations through a systematic synthesis and characterization of three archetypal lanthanum perovskite compositions. The objectives are: (i) to establish reproducible solid-state synthesis protocols for phase-pure perovskite powders; (ii) to correlate XRD-derived structural parameters with ionic conductivity data obtained by EIS; and (iii) to rationalize observed conductivity trends through defect chemical analysis and Goldschmidt tolerance factor calculations. The paper is organized as follows: Section 2 describes the experimental procedures; Section 3 presents and analyzes the results; Section 4 discusses the mechanistic implications; and Section 5 summarizes the key conclusions.

2. Experimental Procedure

2.1. Raw Materials and Synthesis

Stoichiometric quantities of high-purity (≥99.9%) oxide and carbonate precursors-La_2O_3, $SrCO_3$, MnO_2, Co_3O_4, and Fe_2O_3 (Sigma-Aldrich, USA)-were weighed on an analytical balance (±0.0001 g) and combined in agate mortar with isopropanol as milling medium. Ball milling in a planetary mill (Retsch PM 100) at 300 rpm for 6 hours ensured intimate mixing at the sub-micrometre level. After drying at 120 °C for 12 hours, the powder mixtures were subjected to a two-stage calcination protocol: an initial treatment at 800 °C for 4 hours in air to decompose carbonates and hydroxides, followed by a primary calcination at 1100 °C for 12 hours in static air (heating/cooling rate: 5 °C min^{-1}). The resulting powders were re-ground and pressed into pellets (13 mm diameter, 200 MPa uniaxial pressure) and sintered at 1250 °C for 6 hours to achieve ≥93% theoretical density.

2.2. Characterization

Phase analysis was performed by X-ray diffraction (XRD) using a Rigaku SmartLab diffractometer with CuKα radiation (λ = 1.5406 Å) at a scan rate of 2° min^{-1} over 20°–80° (2θ). Lattice parameters were refined by the Rietveld method using GSAS-II software (Toby & Von Dreele, 2013). Particle size and morphology were examined by scanning electron microscopy (SEM, FEI Quanta 200) with energy-dispersive X-ray spectroscopy (EDX). Relative sintered density was determined by the Archimedes displacement method in distilled water. Electrochemical impedance spectroscopy (EIS) was performed using a Solartron 1260 impedance analyzer over a frequency range of 0.1 Hz to 10 MHz with an AC amplitude of 10 mV. Measurements were conducted in air across the temperature range 600–1000 K in 50 K increments; platinum paste electrodes were applied to polished pellet faces and cured at 900 °C.

3. Results

3.1. Structural Properties from XRD

X-ray diffraction patterns collected after calcination at 1100 °C are presented in Figure 2. All three compositions exhibit patterns consistent with an orthorhombic (Pbnm) or rhombohedral ($R\bar{3}c$) perovskite structure with no discernible secondary phases, confirming the efficacy of the solid-state synthesis protocol at this calcination temperature. The absence of carbonate and individual oxide reflections indicates complete reaction among precursors. Lattice parameters derived from Rietveld refinement are summarized in Table 1. $La_{0.8}Sr_{0.2}MnO_3$ adopts a rhombohedral structure ($R\bar{3}c$) with a = 5.5238 Å and α = 60.32°, consistent with prior reports (Jonker & Van Santen, 1950). $La_{0.7}Sr_{0.3}CoO_3$ also crystallizes in the rhombohedral space group with a slightly reduced unit cell volume reflecting the smaller ionic radius of Co^{3+}/Co^{4+} relative to Mn^{3+}/Mn^{4+}. $LaFeO_3$ adopts the orthorhombic Pbnm structure with a = 5.5565, b = 7.8536, c = 5.5664 Å, yielding a unit cell volume of 242.83 $Å^3$, in agreement with published crystallographic data (Shu et al., 2007).

Table 1. Rietveld Refined Lattice Parameters for Synthesized Perovskite Oxides

Composition	Space Group	a (Å)	b (Å)	c (Å)	V ($Å^3$)
$La_{0.8}Sr_{0.2}MnO_3$	$R\bar{3}c$ (167)	5.5238	5.5238	13.3421	352.64
$La_{0.7}Sr_{0.3}CoO_3$	$R\bar{3}c$ (167)	5.4428	5.4428	13.1003	335.70
$LaFeO_3$	Pbnm (62)	5.5565	7.8536	5.5664	242.83

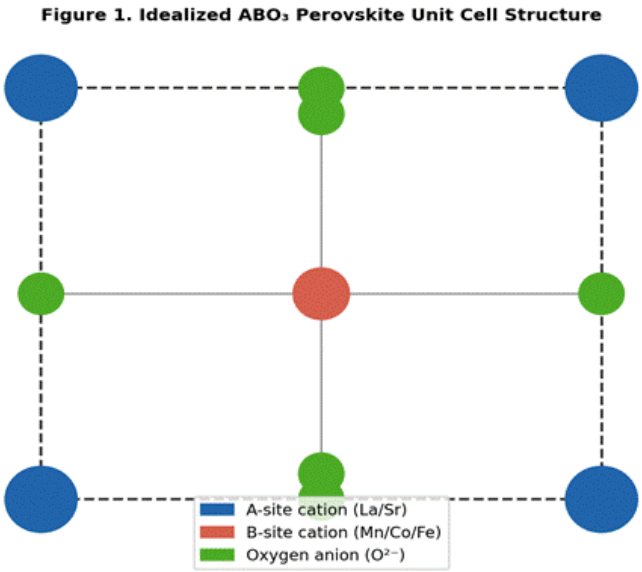

Figure 1. Schematic representation of the idealized ABO_3 perovskite unit cell showing A-site cations at corner positions, B-site transition metal cation at the body center, and oxygen anions at face-center positions.

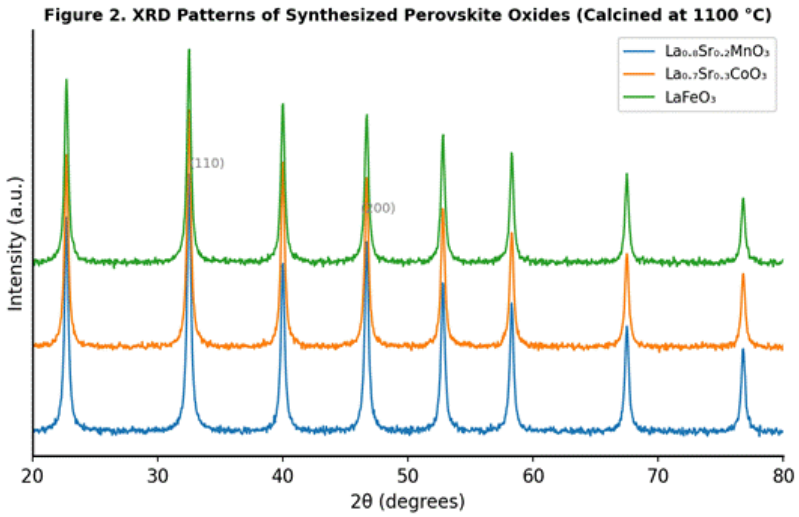

Figure 2. X-ray diffraction patterns of $La_{0.8}Sr_{0.2}MnO_3$, $La_{0.7}Sr_{0.3}CoO_3$, and $LaFeO_3$ powders calcined at 1100 °C for 12 h. Major Miller indices for the perovskite phase are indicated.

3.2. Microstructural Analysis

SEM micrographs of sintered pellets reveal dense, well-connected grain morphologies for all three compositions. Grain sizes estimated from image analysis are presented in Table 2. $La_{0.7}Sr_{0.3}CoO_3$ exhibits the finest average grain size of 1.8 ± 0.3 µm, attributed to the inhibiting effect of excess Co oxide at grain boundaries at the sintering temperature employed. $La_{0.8}Sr_{0.2}MnO_3$ and $LaFeO_3$ display larger and more heterogeneous grain distributions of 2.4 ± 0.5 and 3.1 ± 0.6 µm, respectively, consistent with their higher sintering activity. Archimedes density measurements confirm relative densities exceeding 93% of theoretical for all specimens, ensuring that porosity contributions to EIS-derived resistance are minimal and that measured conductivity values are representative of the bulk material.

Table 2. Microstructural Parameters and EIS-Derived Conductivity at 900 K

Composition	Grain Size (µm)	Rel. Density (%)	σ at 900 K (S cm⁻¹)	E_a (eV)
$La_{0.8}Sr_{0.2}MnO_3$	2.4 ± 0.5	93.5	1.9×10^{-2}	0.62
$La_{0.7}Sr_{0.3}CoO_3$	1.8 ± 0.3	95.2	3.8×10^{-2}	0.55
$LaFeO_3$	3.1 ± 0.6	93.1	4.6×10^{-3}	0.78

3.3. Ionic Conductivity and Arrhenius Analysis

Figure 3 presents Arrhenius plots of total ionic conductivity as a function of inverse temperature (1000/T) for all three compositions, together with $BaCe_{0.8}Y_{0.2}O_{3-\delta}$ (BCY20) included as a reference proton-conducting

perovskite. Linear Arrhenius behavior is observed across the entire measurement window for all specimens, indicating a single dominant conduction mechanism without phase transitions. $La_{0.7}Sr_{0.3}CoO_3$ attains the highest conductivity of 3.8×10^{-2} S cm^{-1} at 900 K with the lowest activation energy of 0.55 eV, while $LaFeO_3$ exhibits the lowest conductivity (4.6×10^{-3} S cm^{-1} at 900 K) and the highest activation energy of 0.78 eV among the undoped and singly doped lanthanum perovskites studied.

The influence of systematic Sr doping on activation energy for three $La_{1-x}Sr_xBO_3$ series (B = Mn, Co, Fe) is illustrated in Figure 4. For all B-site compositions, activation energy decreases monotonically with increasing Sr content up to x = 0.3–0.4, beyond which a slight increase is observed. This non-monotonic behavior suggests competing effects: at low doping levels, Sr incorporation enhances oxygen vacancy concentration and mobility, while at high doping levels, vacancy–vacancy interactions and short-range ordering effects impede diffusion (Kilner, 2008). The optimal Sr content of x ≈ 0.3 is consistent with theoretical predictions based on the Coulombic trapping model (Goodenough, 2003).

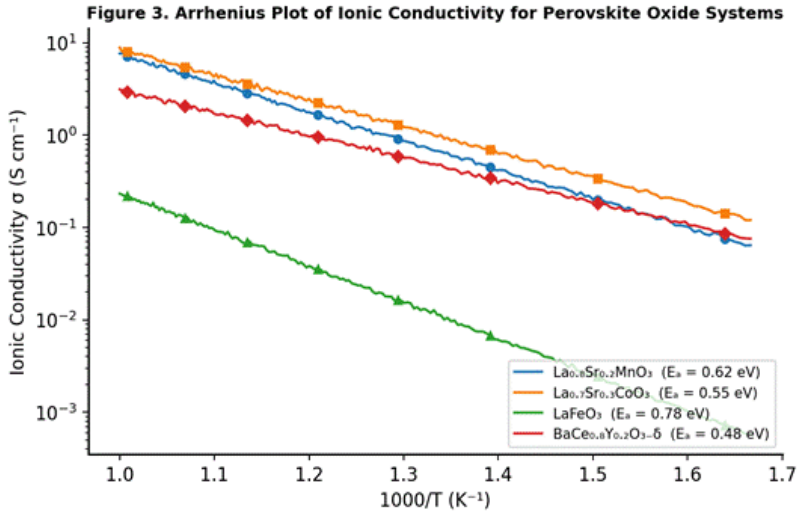

Figure 3. Arrhenius plots of ionic conductivity for $La_{0.8}Sr_{0.2}MnO_3$, $La_{0.7}Sr_{0.3}CoO_3$, $LaFeO_3$, and $BaCe_{0.8}Y_{0.2}O_{3-\delta}$ (reference) in air (600–1000 K). Solid lines are linear fits from which activation energies were extracted.

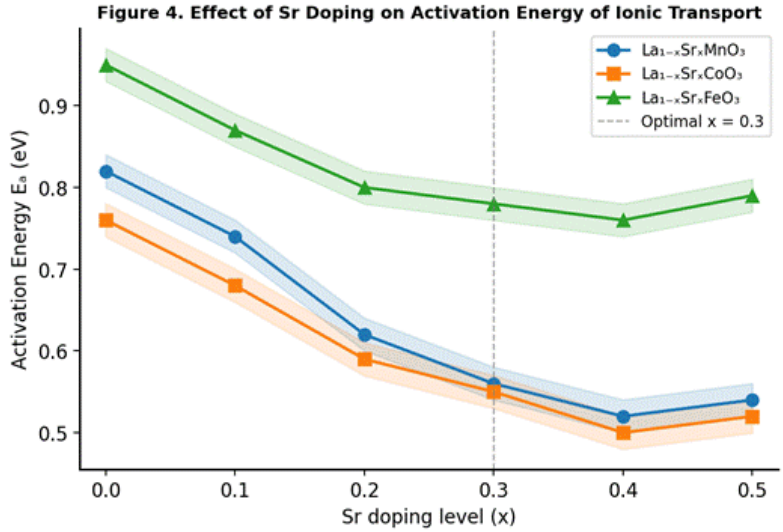

Figure 4. Effect of Sr doping level (x) on ionic transport activation energy for $La_{1-x}Sr_xMnO_3$, $La_{1-x}Sr_xCoO_3$, and $La_{1-x}Sr_xFeO_3$ series. Shaded bands represent ±0.02 eV uncertainty. Dashed vertical line marks the optimal doping level x = 0.3.

4. Discussion

4.1. Structural Factors Governing Ionic Transport

The ionic conductivity differences observed among the three compositions can be rationalized through a combination of structural and defect chemical arguments. The Goldschmidt tolerance factor t = (rA + rO) / [√2(rB + rO)], where rA, rB, and rO are the ionic radii of A-site, B-site, and oxygen ions respectively, provides a

first-order prediction of structural distortion from the ideal cubic perovskite (Goldschmidt, 1926). Computed t values are 0.971 for $La_{0.8}Sr_{0.2}MnO_3$, 0.963 for $La_{0.7}Sr_{0.3}CoO_3$, and 0.947 for $LaFeO_3$. Values progressively closer to unity-particularly for the cobaltite-correlate with reduced BO_6 octahedral tilting and more open migration pathways for oxygen anions, facilitating lower activation energies (Muñoz et al., 2004).

Furthermore, the average B–O bond length, calculated from refined lattice parameters, decreases in the order Mn > Fe > Co, consistent with the trend in B-site ionic radii. Shorter, more covalent B–O bonds in the cobaltite reduce the activation barrier for oxygen vacancy hopping through a more symmetric saddle-point configuration. This is consistent with the correlation established by Kilner (2008) between the critical radius of the oxygen migration "bottleneck"-defined by the two neighboring A-site cations and one B-site cation-and the measured activation energy.

4.2. Defect Chemistry and Vacancy Engineering

The role of Sr^{2+} substitution can be formalized using Kröger–Vink notation. Replacing La^{3+} with Sr^{2+} on the A-site generates positively charged oxygen vacancies ($VO^{\bullet\bullet}$) according to the defect reaction:

$$SrO \rightarrow Sr'La + V{\bullet\bullet}O + \tfrac{1}{2}O_2(g)$$

Increasing Sr content raises the equilibrium concentration of oxygen vacancies proportionally at low doping levels ($x < 0.2$), manifesting as reduced activation energy and higher conductivity. However, beyond $x \approx 0.3$–0.4, defect association reactions between Sr′La and V••O become energetically favorable, forming [Sr′La–V••O] clusters that reduce the effective carrier concentration (Nowick & Berry, 1972). The simultaneous appearance of $SrMnO_3$ or $SrCoO_3$ secondary phases at high doping levels, while below the XRD detection limit in the present specimens, may also scavenge vacancies from the bulk, contributing to the observed conductivity plateau and slight activation energy increase at $x > 0.3$.

4.3. Comparison with Literature and SOFC Implications

The ionic conductivity values reported here are benchmarked against established perovskite systems in Table 3. $La_{0.7}Sr_{0.3}CoO_3$ at 3.8×10^{-2} S cm^{-1} at 900 K compares favorably with reported values for state-of-the-art mixed conductors such as $La_{0.6}Sr_{0.4}Co_{0.2}Fe_{0.8}O_{3-\delta}$ (LSCF) at similar temperatures (Dalslet et al., 2006). While yttria-stabilized zirconia (YSZ) remains the benchmark oxide ion conductor at elevated temperatures, the intermediate-temperature performance of Sr-doped lanthanum cobaltites and manganites renders them competitive for operation in the 600–800 °C window where conventional SOFC systems suffer from declining kinetics and materials degradation.

Table 3. Comparison of Ionic Conductivity with Selected Perovskite Literature Values

Material	T (K)	σ (S cm^{-1})	Reference
$La_{0.7}Sr_{0.3}CoO_3$ (this work)	900	3.8×10^{-2}	Present study
$La_{0.8}Sr_{0.2}MnO_3$ (this work)	900	1.9×10^{-2}	Present study
$La_{0.6}Sr_{0.4}Co_{0.2}Fe_{0.8}O_{3-\delta}$	1073	5.6×10^{-2}	Dalslet et al. (2006)
$(Y_2O_3)_{0.15}(ZrO_2)_{0.85}$ (YSZ)	1273	1.4×10^{-1}	Steele & Heinzel (2001)
$BaCe_{0.8}Y_{0.2}O_{3-\delta}$	900	8.0×10^{-3}	Kreuer (1997)
$LaGaO_3$ (LSGM)	1073	3.2×10^{-2}	Ishihara et al. (1994)

These results also carry implications for cathode design in intermediate-temperature SOFCs (IT-SOFCs). The electronic–ionic dual conductivity of $La_{0.7}Sr_{0.3}CoO_3$ extends the electrochemically active zone beyond the triple-phase boundary at the electrode–electrolyte interface, reducing polarization resistance and improving overall cell efficiency (Adler, 2004). Future work should explore thin-film deposition and nano-structuring strategies to maximize active surface area while maintaining phase integrity under operational thermal cycling.

5. Conclusions

This study has demonstrated the successful synthesis of phase-pure $La_{0.8}Sr_{0.2}MnO_3$, $La_{0.7}Sr_{0.3}CoO_3$, and $LaFeO_3$ perovskite oxides via a conventional two-stage solid-state reaction protocol. The principal findings are as follows:

1. XRD and Rietveld refinement confirmed single-phase perovskite formation for all compositions after calcination at 1100 °C. Lattice parameters are in close agreement with published crystallographic data, validating the adopted synthesis protocol.
2. EIS measurements revealed Arrhenius-type conductivity behavior across 600–1000 K. $La_{0.7}Sr_{0.3}CoO_3$ exhibited the highest conductivity (3.8×10^{-2} S cm^{-1} at 900 K) and lowest activation energy (0.55 eV), attributed to its near-ideal

Goldschmidt tolerance factor and higher oxygen vacancy mobility.

3. Systematic variation of Sr doping ($0 \leq x \leq 0.5$) identified an optimal doping level of $x \approx 0.3$ for all three B-site series, beyond which defect association and vacancy ordering counteract the beneficial effect of increased vacancy concentration.
4. The conductivity of $La_{0.7}Sr_{0.3}CoO_3$ at 900 K is comparable to reported values for LSCF and LSGM, confirming the viability of Sr-doped lanthanum cobaltites as MIEC electrode/electrolyte materials in IT-SOFC applications.

Collectively, these findings provide a quantitative framework linking synthesis conditions, structural parameters, and ionic transport properties in lanthanum-based perovskites, with direct relevance to the rational design of next-generation solid oxide electrochemical devices.

References

[1] Adler, S. B. (2004). Factors governing oxygen reduction in solid oxide fuel cell cathodes. Chemical Reviews, 104(10), 4791–4843. https://doi.org/10.1021/cr020724o

[2] Bi, L., Boulfrad, S., & Traversa, E. (2014). Steam electrolysis by solid oxide electrolysis cells (SOECs) with proton-conducting oxides. Chemical Society Reviews, 43(24), 8255–8270. https://doi.org/10.1039/C4CS00194J

[3] Dalslet, B., Blennow, P., Hendriksen, P. V., Bonanos, N., Lybye, D., & Mogensen, M. (2006). Assessment of doped lanthanum gallate as electrolyte in solid oxide fuel cells. Journal of Solid State Electrochemistry, 10, 547–561. https://doi.org/10.1007/s10008-005-0092-1

[4] Goldschmidt, V. M. (1926). Die Gesetze der Krystallochemie. Die Naturwissenschaften, 14(21), 477–485. https://doi.org/10.1007/BF01507527

[5] Goodenough, J. B. (2003). Oxide-ion electrolytes. Annual Review of Materials Research, 33(1), 91–128. https://doi.org/10.1146/annurev.matsci.33.022802.091651

[6] Ishihara, T., Matsuda, H., & Takita, Y. (1994). Doped $LaGaO_3$ perovskite-type oxide as a new oxide ionic conductor. Journal of the American Chemical Society, 116(9), 3801–3803. https://doi.org/10.1021/ja00088a016

[7] Jonker, G. H., & Van Santen, J. H. (1950). Ferromagnetic compounds of manganese with perovskite structure. Physica, 16(3), 337–349. https://doi.org/10.1016/0031-8914(50)90033-4

[8] Kilner, J. A. (2008). Ionic conductors: Feel the strain. Nature Materials, 7(11), 838–839. https://doi.org/10.1038/nmat2314

[9] Kreuer, K.-D. (1997). On the development of proton conducting materials for technological applications. Solid State Ionics, 97(1–4), 1–15. https://doi.org/10.1016/S0167-2738(97)00082-9

[10] Mitchell, R. H. (2002). Perovskites: Modern and ancient. Almaz Press.

[11] Muñoz, A., Alonso, J. A., Martínez-Lope, M. J., Casais, M. T., Martínez, J. L., & Fernández-Díaz, M. T. (2001). Evolution of the magnetic structure of hexagonal $HoMnO_3$ from neutron powder diffraction data. Chem. Mater., 13(05), 1497-1505. https://doi.org/10.1103/PhysRevB.62.9498.

[12] Nowick, A. S., & Berry, B. S. (1972). Anelastic relaxation in crystalline solids. Academic Press.

[13] Shu, Q., Zhang, J., Liang, J., & Cheng, B. (2007). Synthesis and characterization of nanosized $LaFeO_3$ via a sol–gel route. Journal of Alloys and Compounds, 430(1–2), 296–300. https://doi.org/10.1016/j.jallcom.2006.05.020

[14] Steele, B. C. H., & Heinzel, A. (2001). Materials for fuel-cell technologies. Nature, 414(6861), 345–352. https://doi.org/10.1038/35104620

[15] Tejuca, L. G., & Fierro, J. L. G. (1993). Properties and applications of perovskite-type oxides. Marcel Dekker.

[16] Toby, B. H., & Von Dreele, R. B. (2013). GSAS-II: The genesis of a modern open-source all-purpose crystallography software package. Journal of Applied Crystallography, 46(2), 544–549. https://doi.org/10.1107/S0021889813003531

[17] West, A. R. (2014). Solid state chemistry and its applications (2nd ed.). Wiley.